High Thermoelectric Performance of a Heterogeneous PbTe Nanocomposite

Hongchao Wang,[†,⊥] Junphil Hwang,[†,⊥] Matthew Loren Snedaker,[‡] Il-ho Kim,[§] Chanyoung Kang,[†] Jungwon Kim,[†] Galen D. Stucky,[‡,‖] John Bowers,[‖] and Woochul Kim*,[†]

[†]School of Mechanical Engineering, Yonsei University, Seoul 120-749, Korea

[‡]Department of Chemistry & Biochemistry, University of California, Santa Barbara, Santa Barbara, California 93106, United States

[§]Department of Materials Science and Engineering, Korea National University of Transportation, 50 Daehangno, Chungju, Chungbuk 380-702, Korea

[‖]Materials Department, University of California, Santa Barbara, Santa Barbara, California 93106, United States

Ⓢ Supporting Information

ABSTRACT: In this paper, we propose a heterogeneous material for bulk thermoelectrics. By varying the quenching time of Na doped PbTe, followed by hot pressing, we synthesized heterogeneous nanocomposites, a mixture of nanodot nanocomposites and nanograined nanocomposites. It is well-known that by putting excess amounts of Na (i.e., exceeding the solubility limit) into PbTe, nanodots with sizes as small as a few nanometers can be formed. Nanograined regions with an average grain size of ca. 10 nm are observed only in materials synthesized with an extremely low quenching rate, which was achieved by using a quenching media of iced salt water and cold water. Dimensionless thermoelectric figures of merit, zT, of those heterogeneous nanocomposites exhibited a zT around 2.0 at 773 K, which is a 25% increase compared to zT of a homogeneous nanodot nanocomposite with the largest quenching time in our experiment, i.e. furnace cooled. The power factor increase is 5%, and the thermal conductivity reduction is 15%; thus, zT increase mainly comes from the thermal conductivity reduction.
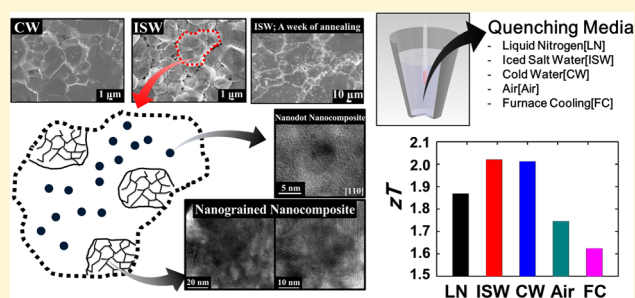
■ INTRODUCTION

Thermoelectric energy conversion can directly convert heat into electricity or vice versa.[1−3] Thermoelectrics are scalable and reliable, but their application for waste heat recovery from automotive, power plant, industrial waste heat, and body heat requires improvement in thermoelectric conversion efficiency. The conversion efficiency of the thermoelectric device is proportional to the dimensionless thermoelectric figure of merit, $zT = [S^2/\rho(\kappa_l+\kappa_e)]T$, where T is the absolute temperature, S is the Seebeck coefficient, ρ is the electrical resistivity, and κ_l and κ_e are the lattice and electronic thermal conductivities, respectively. It is obvious that zT can be enhanced either by maximizing the power factor, S^2/ρ, and/or by minimizing thermal conductivity, κ. As shown in the expression, the zT is composed of purely material properties, so the choice of right material in a designated temperature range ensures high conversion efficiency.

As reviewed in several articles,[3−5] there has been active research on thermoelectrics after Hicks and Dresselhaus's[6,7] papers in 1993 where they proposed nanostructured materials for high zT. Indeed, these efforts led to an increase in the dimensionless thermoelectric figure of merit beyond ~2 and can be categorized into two different approaches: band engineering for the power factor increase and nanostructuring

for the thermal conductivity reduction. An example of power factor enhancement by band engineering was demonstrated by Heremans et al.,[8] who showed that the Seebeck coefficient can be increased due to the distortion of the electronic density of states created by impurity atoms—thallium in their study—in PbTe, yielding $zT \sim 1.5$ at 773 K. This study proved a concept suggested by Mahan and Sofo,[9] who suggested that the Seebeck coefficient can be enhanced if there exists a local increase in the density of states over a narrow energy range (i.e., a resonant level). Pei et al.[10] proposed another example of power factor enhancement by band engineering through the convergence of many valence (or conduction) valleys for a simultaneous increase in Seebeck coefficient and electrical conductivity. They achieved this by tuning the doping and composition in bulk PbTe and showed a zT value of 1.8 at about 850 K.

It is known that interfaces and boundaries of nanostructures scatter phonons and thereby reduce the thermal conductivity and increase the thermoelectric figure of merit.[11−13] In bulk materials, two different types of nanocomposites were used for the zT increase—nanodot nanocomposites[14,15] and nanograined

nanocomposites.[16] Nanodot nanocomposites contain nano-structures embedded in a host material and generally consist of single crystals. The figures of merit for Na doped PbTe alloys were about 1.6, 1.5, 1.3, and 1.7 for insertion of Mg_2Te,[17] CaTe and BaTe,[18] and strained endotaxial SrTe nanostructures,[15] respectively. Recently, Biswas et al.[14] reported a dimensionless figure of merit as 2.2 at 915 K in 2 mol % Na doped PbTe-SrTe alloys synthesized by spark-plasma-sintering (SPS). The increase in zT was attributed to the lower thermal conductivity by 'all-scale hierarchical architectures' — alloy atoms for scattering high frequency phonons, nanodots for scattering mid- frequency phonons, and mesoscale grains for scattering low frequency phonons. Nanograined nanocomposites are polycrystalline materials, with grain sizes on the order of 1−100 nm. Poudel et al.[16] reported a peak zT of 1.4 at 100 °C in a p-type nanocrystalline BiSbTe bulk alloy. They attributed the zT increase to phonon scattering by 2 to 10 nm grains.

In this study, we propose a heterogeneous nanocomposite—mixture of the nanodot nanocomposite and the nanograined nanocomposites—as a route for enhancing zT of a material. In this case, nanodots only form inside the nanodot nanocomposite and nanosized grains only exist in the nanograined nanocomposite. It is known that thermal conductivity of the heterogeneous material is less than that of the volume averaged thermal conductivity due to the heterogeneous temperature gradient.[19−21] In addition to this, the mean distance between particles should be reduced because under a fixed nanodot concentration, nanodots have to reside in a more confined region compared to the homogeneous nanocomposites; therefore, phonon scattering due to nanodots increases so thermal conductivity decreases. Previously, Kang et al.[22] compared thermal conductivities of nanodot nanocomposites and nanograined nanocomposites and concluded that the nanograined nanocomposite could achieve lower thermal conductivity than the nanodot nanocomposite as long as the nanograined nanocomposite has a sufficiently small grain size (i.e., a few nanometers in size). In our case, we found that, in the heterogeneous nanocomposite, there are regions where grains with a few nanometers in size and where nanodots resides, which led to a thermal conductivity reduction.

Lead telluride (PbTe) with a NaCl-type crystal structure is one of the most promising thermoelectric materials in the temperature range of 600 to 900 K.[8,10,13−15,18,23−26] We previously reported zT ~1.7 at 773 K for $Pb_{0.98}Na_{0.02}Te$ by optimizing the hot pressing conditions.[25] Later, we further enhanced the zT to 2.0 at 773 K by quenching the PbTe melt followed by the optimized hot pressing conditions.[23] In this paper, we varied the quenching medium from liquid N_2 (LN), iced salt water (ISW), cold water (CW), air cooling (Air), to furnace cooling (FC) to study the effects of quenching rate on thermoelectric properties. We intended to form nanodots by putting excess amount of Na (i.e., exceeding the solubility limit) into PbTe.[26] We found that the dimensionless figure of merit increased from 1.6 to 2.0 by increasing the quenching rate from FC to ISW, except for LN. An inhomogeneous mixture of the nanodot nanocomposites and nanograined nanocomposites were observed only in the ISW and CW samples. We attributed the low thermal conductivity of these materials as the main reason for such an increase in zT.

■ RESULTS AND DISCUSSION

Samples of $Pb_{0.98}Na_{0.02}Te$ were synthesized by melting, quenching, and hot pressing (see Figure 1). High purity
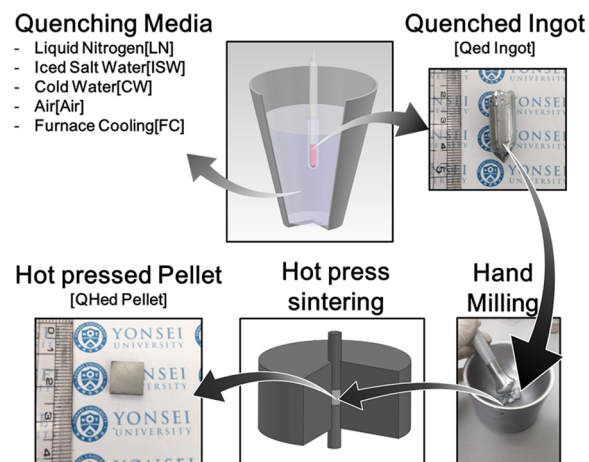
Figure 1. A schematic showing material synthesis processes. The quenching media were liquid nitrogen (LN), iced salt water (ISW), cold water (CW), room air (Air), and air inside the furnace (FC). The Qed ingot and QHed pellet are denoted as quenched ingot and a hot pressed pellet of the Qed ingot, respectively.

starting elements of lead (Pb, 3N, Alfa Aesar), tellurium (Te, 4N, Alfa Aesar), and sodium (Na, 99.95%, Alfa Aesar) were used for the reaction. They were mixed in stoichiometric proportion and put into a carbon-coated quartz tube under N_2 atmosphere in a glovebox. The tube was flame-sealed under a pressure of approximately 10^{-4} Torr. The reaction mixtures were heated to 1073 K for 2 h followed by melting at 1273 K for 6 h. Then, the mixtures were quenched. To vary the quenching rate, we used the different quenching media of liquid N_2 (LN), iced salt water (ISW), cold water (CW), and room air (Air) as well as natural cooling in the reaction furnace (FC). The quenching time, the time for the reaction mixture to reach room temperature, was roughly estimated with the lumped capacitance approximation to be about 6, 15, and 30 s for LN, ISW, and CW, respectively as presented in Figure S2 in the Supporting Information. The quenching times for air quenching and furnace cooling were measured approximately to be about 0.5 and 8 h, respectively. We found blankets of vapors wrapping around the quartz tube especially in liquid nitrogen quenching, which should inhibit heat transfer between the liquid nitrogen and the sample. Therefore, the actual quenching time should be slower than the estimated time.[27] After the quenching, the ingots were then ground into powder and subsequently hot-pressed at 100 MPa at 773 K for 1 h. Electrical heaters supplied heat in the hot pressing machine. The hot pressing condition used was based on an optimized condition for this material obtained in our previous work.[25] For comparison purposes, the grounded powders were also spark-plasma-sintered (SPSed) as well. The SPS conditions we used were similar to that of the reference paper by Biswas et al.[14] (i.e., 50 MPa at 773 K for 10 min). The pellet with a relative density of 99% or higher was used for simultaneous measurements of the thermoelectric properties.

Cross-sectional morphology was observed using a JSM-6701F scanning electron microscope (SEM) by looking at the fractured surface of samples. Transmission election microscopy (TEM) was carried out using a JEM-2100F microscope. Specimens for TEM were prepared by a focused ion beam (FIB) using a milling power below 5 keV as suggested by Baram and Kaplan.[28] An ULVAC ZEM-3 was used to measure electrical resistivities and Seebeck coefficients simultaneously

during heating from room temperature to 800 K. Thermal diffusivity was measured with a laser flash apparatus (Netzsch LFA 457). Heat capacity was estimated by the relationship, C_p (k_B per atom) = $3.07 + 4.7 \times 10^{-4} \times (T/\text{K-300})$, which was obtained by fitting the experimental data reported by Blachnik and Igel.[29] The thermal conductivity, κ, was extracted from the thermal diffusivity, λ, the specific heat capacity, C_p, and the density, d, based on the relationship $\kappa = \lambda C_p d$. Here, the density was measured by Archimedes' method. The data of density is shown in Table S1. The dimensionless figure of merit was then calculated from the measured thermoelectric parameters. The crystal structure analysis of each samples was done by powder X-ray diffraction (XRD) with Cu Kα radiation using Rigaku powder X-ray diffractometer. The result is shown in Fig S1.

We performed theoretical calculations focusing on the lattice thermal conductivity. The lattice thermal conductivities were deduced based on the Wiedemann–Franz law using the Lorenz number that we have calculated in our previous study.[23] In the paper, the Lorenz number was calculated based on the linearized Boltzmann transport equation (BTE) with an approximate relaxation time considering convergence of valence bands. The lattice thermal conductivity was calculated using Callaway's model.[30] The details for simulating the Lorenz number and Callaway's model are available elsewhere,[11,12,22,23,30,31] so it will not be repeated here. Effective thermal conductivity should be calculated in a material containing regions of different thermal conductivities. Parrott and Stuckes reviewed[32] treatments on these cases. In this study, we used the following relationship suggested by Klemens et al.[19−21] to calculate the effective thermal conductivity, κ_{eff}

$$\kappa_{eff} = \kappa_0 - \frac{1}{\kappa_0} \sum_q \cos^2\theta \, |\kappa(q)|^2 \qquad (1)$$

where κ_0 is the volume-averaged thermal conductivity, κ is the thermal conductivity as a function of a wave-vector q, and θ is the angle between each q and the direction of the average temperature gradient. In our case, the nanodot nanocomposites and the nanograined nanocomposites are distributed randomly, so we assume that they are isotropically dispersed. In this case, the effective thermal conductivity can be expressed as follows[19−21]

$$\kappa_{eff} = \kappa_0 - \frac{1}{3\kappa_0 V_0} \int [\kappa(r) - \kappa_0]^2 \, dr \qquad (2)$$

where $\kappa(r)$ is the thermal conductivity as a function of position r, and V_0 is the volume of the domain of the integration.

Figure 2 shows micro- and nanostructures of the samples. Scanning electron microscope (SEM) images of as-quenched ingots (i.e., Qed Ingot) are shown in Figure 2(a). Except for the furnace-cooled sample (FC), morphologies of all samples look similar; there are many tiny blobs throughout. The density of the tiny blobs is higher in the ISW and CW samples than in the others. Interestingly, these tiny blobs survived even after the hot pressing only in the ISW and CW samples as shown in Figure 2(b), where the SEM images of the hot pressed pellets of the quenched ingot (i.e., QHed pellets) are shown. Looking at these tiny blobs under the transmission electron microscope (TEM) in Figure 3 reveals that they consist of nanosized grains around 10 nm in size (i.e., the tiny blobs constitute the nanograined nanocomposite). As shown in Figure 2(b), the grain size of each samples increases when decreasing the quenching rate, except for the LN case. During the quenching
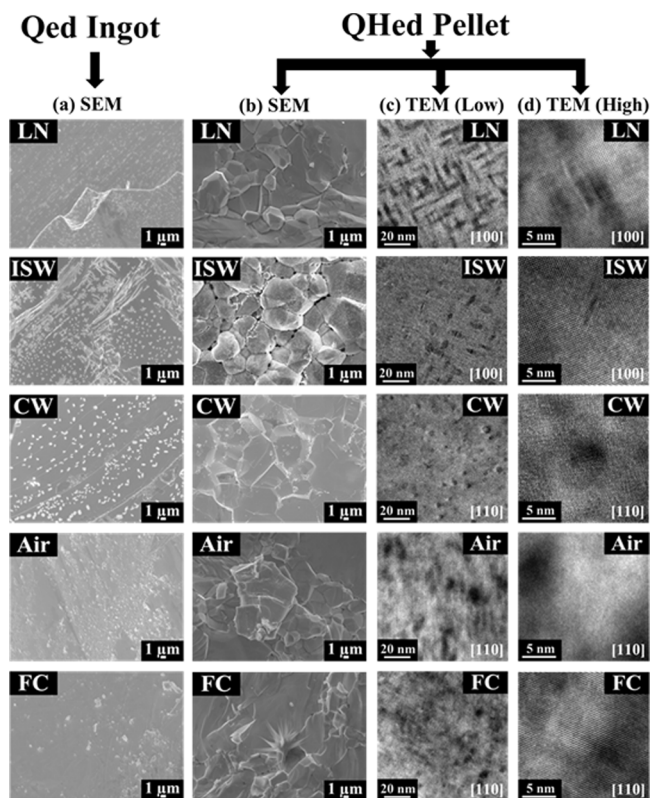
Figure 2. Micro- and nanostructures of samples. (a) SEM images of as quenched ingot (Qed ingot). (b) SEM images of the pellets obtained by hot pressing the Qed ingots (QHed pellet). (c) The low magnification and (d) high magnification TEM images of the QHed pellets probing the nanodot nanocomposite.
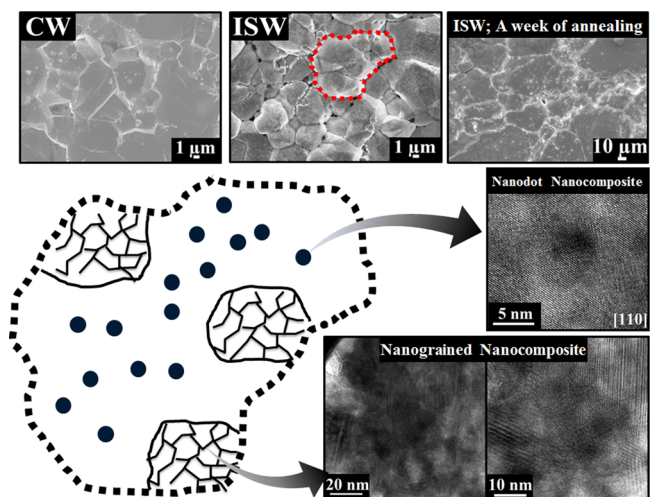
Figure 3. A schematic diagram showing heterogeneous nanocomposite, a mixture of nanograined and nanodot nanocomposites; inside the ∼10 μm grain, there exists a region with nanosized grains and a region containing nanodots. The tiny blobs in SEM images of CW and ISW turned out to be a region composed of nanosized grains around 10 nm in size as shown in the TEM images at the bottom. Also, these blobs did not disappear even after 1 week of annealing at 773 K, as shown in the SEM image.

process, we found the quenching rate of LN is slower than that of CW and ISW. In the liquid nitrogen quenching (LN), blankets of vapors generated during the quenching process blocked heat transfer between the liquid nitrogen and the

molten sample, which should delay the quenching process leading increased grain sizes. In the Air and FC cases, grains greater than >100 μm coexist with midsized (~10 μm) grains. For the cold water (CW) and ISW samples, variation in grain size is large; there are 20−60 μm sized grains and <10 μm sized grains. Figure 2(c) and (d) show the low and high magnification images of TEM. In the TEM images, precipitated nanostructures are clearly observable. According to previous reports,[14,33,34] the 2% mole fraction of Na is already beyond the solubility limit of Na in PbTe. Thus, excessive Na atoms tend to form nanoscale precipitates in the form of Na_2Te or accumulate at the grain boundaries or defect sites. We found the shape of the precipitates depends on the zone axis. In the LN samples, for example, the precipitates are platelet shaped at the [100] zone axis, but at the [110] and [111], the shape is rounded or ellipsoidal. Therefore, the shape of the precipitation is platelet-like, but it looks different depending on the direction where it is being looked at, which is consistent with observations by He et al.[34] The bright field (BF) and high angle annular dark field (HAADF) images in Figure S3 in the Supporting Information confirmed that the contrast in the TEM image is caused by compositional differences. Also, we deduced the lattice constant based on high resolution TEM images and found that the lattice constant in the nanodot region is smaller than that of the PbTe matrix, which is also consistent with findings by He et al.[34] It was Na rich precipitation revealed in recent studies.[14,34,35]

Figure 3 shows a schematic of the heterogeneous nanocomposite, a mixture of nanodot nanocomposite and nano-grained nanocomposite, along with SEM and TEM images. We observed this heterogeneous nanocomposite only in the ISW and CW samples, but we cannot rule out the existence of this in other samples as well. The tiny blobs in Figure 2(a) and (b) turned out to be a region composed of nanosized grains around 10 nm in size. Also, these blobs did not disappear even after 1 week of annealing at 773 K, as shown in the SEM image in Figure 3. According to the energy dispersive X-ray spectroscopy (EDS) analysis, we found the nanograined region is Te rich, Pb:Te = 4:6. The fact that the blobs survived a week of annealing at 773 K might rule out the possibility of existence of pure Te. The Na, which was not detected by the EDS analysis, probably due to the resolution limit of the EDS, may exist inside the grain. Since we have looked at small TEM specimens, further rigorous investigation is required to figure out the exact composition for this nanograined region. Although further study is needed to understand why the nanograined region was observed in samples with low quenching rate, our hypothesis is as follows. In general, in the case of quenching, nucleation site is small and activation energy for grain growth is large, which could lead to the generation of a nanograined region as observed in the "as-quenched ingot". During the hot pressing, as the excess Na precipitated to the Na−Te compound, to relieve the strain generated due to the lattice mismatch between the matrix, the Na−Te compound may give a chance for those nanograined regions to be stable. As shown in the schematic in Figure 3, the material is highly heterogeneous; inside the ~10 μm grain, there exists a region with nanosized grains and a region containing nanodots. We did not observe nanodots in the nanosized grains. According to experimental data and theoretical analysis provided later in this paper, thermal transport was reduced in the heterogeneous nanocomposite, yet electrical transport was not significantly affected. In addition to the fact that the thermal conductivity of the heterogeneous

material is less than the volume averaged thermal conductivity,[19−21] the mean spacing between nanodots, which affects phonon mean free path, could be closer than that in the homogeneous material. This is because the precipitated nanodots should only exist in a confined region where there are no nanosized grains.

Figure 4(a) shows temperature dependent values of zT, power factor (PF = S^2/ρ), and thermal conductivity, and Figure
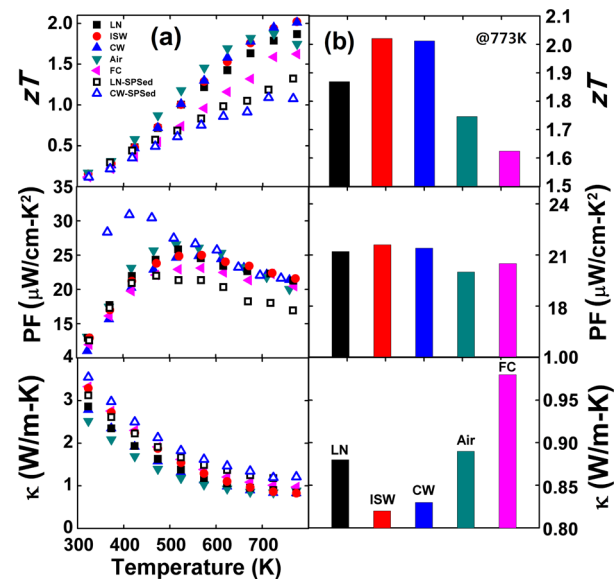
Figure 4. (a) Temperature dependent values of the dimensionless figure of merit, zT, power factor (PF = S^2/ρ), and thermal conductivity of $Pb_{0.98}Na_{0.02}Te$ and (b) zT, PF, and κ at 773 K for various quenching rates.

4(b) represents those at 773 K with various quenching rates. The values shown for the LN, ISW, CW, Air, and FC samples are average values of 6, 6, 13, 2, and 3 measurements, respectively. In Figure 4(a), we also show the thermoelectric properties of the quenched samples that were spark plasma sintered (SPSed) (i.e. LN-SPSed and CW-SPSed) as well for comparison purposes. The zTs of these SPSed samples are consistent with those of Biswas et al.[14] Both the hot-pressing method and the SPS synthesize a sample by applying pressure at elevated temperatures. Although imposing pressure on the sample could be identical for both methods in the case of the uniaxial pressing machine, the ways to apply heat transfer on the sample are different; heat is transferred to the sample by convection and/or radiation in the hot-pressing method, while volumetric heat generation generated inside the sample through the Joule heating occurs in the SPS. Thus, thermal history on the sample by the hot-pressing method depends on convectional and/or radiational−thermal time constant; it takes some time for the sample to reach steady-state temperature. However, the temperature of the SPSed sample does not need to equilibrate surrounding temperature; it can be processed in a short time. In addition to this, the temperature gradient inside the sample during SPS cannot be avoided, yet isothermal condition in the sample can be assumed in the hot-pressing method depending on the synthesis time. Based on this, we have hypothesized that the tiny blobs might have survived even in the larger quenching rate in the SPSed sample owing to the short sintering time, but the reason for deviations in properties between the hot pressed, QHed, and spark plasma

sintered, QSPSed, samples is a subject for future study. It is necessary to find the optimal synthesis condition for the QSPSed samples for a fair comparison.

The dimensionless figure of merit increases as a function of measured temperature up to the limit of our measured temperature range for all samples except the air-quenched sample. The dimensionless figure of merit for the air-quenched sample first increases to a saturation value around 700 K and then slowly drops, which may be due to the increase of bipolar thermal conductivity at high temperature.[23] Electrical resistivities and Seebeck coefficients for the hot pressed specimens are presented in Figure S4. The power factor increases rapidly up to around 500 K due to the rapid increase of Seebeck coefficients with temperature and then slowly decreases with the increase of measured temperature, which is related to the rapid increase of electrical resistivity and saturation of Seebeck coefficient at higher temperatures. In the limit of measured temperature, the values of the power factor for all samples are almost the same. Based on this, we found that the quenching rate does not significantly affect the electrical properties for $Pb_{0.98}Na_{0.02}Te$ alloys, which is also summarized by the PF versus various quenching rates in Figure 4(b).

To understand the reason for this trend in zT, the values of power factors and thermal conductivities of various quenching time are also shown in Figure 4(b). As shown in Figure 4(b), zT does depend on the quenching time, and zTs of ISW and CW at 773 K are around 2.0. We clearly see that the dimensionless figure of merit increases from 1.6 to 2.0 with shorting quenching time except for the LN sample, which may be related to the longer quenching time due to the blanket of vapors generated during the quenching process. Based on percentage variations in the power factor, thermal conductivity, and zT normalized to those of the furnace-cooled sample (FC) as shown in Figure S5, which spans from −2% to 5%, 9% to 15% and from 7% to 25%, respectively, it was deduced that differences in zTs resulted from variances in the thermal conductivities.

The lattice thermal conductivities of the samples are shown in Figure 5. Although the solubility limit of Na in PbTe depends on the synthesis condition and temperature,[26] in our analysis, we assumed that the solubility limit is 0.5% based on the literature value,[33] so the remaining 1.5% should be precipitated in the form of Na_2Te with a diameter of 5.5, 2.4, 2.4, 8.5, and 8.5 nm for the LN, ISW, CW, Air, and FC samples, respectively based on the TEM images in Figure S6. The size distributions of the nanoprecipitates along with the sensitivity analysis are also presented in Figure S6. As shown in the simulated values, lattice thermal conductivities of LN, Air, and FC are almost similar to one another. It is known[23] that, given the same nanodot concentration, the mean size of the nanodot is directly related to the interparticle spacing assuming homogeneous distribution of nanostructures; the smaller the size of the nanostructure, the closer the interparticle spacing. The spacings between the nanodots could be estimated as 12.5, 19.3, and 19.3 nm for the LN, Air, and FC samples, respectively. Therefore, we can deduce that the phonon mean free path of scattering processes other than scattering due to the nanodots should be shorter than 12.5 nm. Lattice thermal conductivities of hot-pressed ISW are presented separately in Figure 5(b). The thermal conductivities of the nanodot nanocomposite were calculated assuming 1.5% of nanodots are homogeneously distributed, and those of the nanograined nanocomposites were simulated with grain size of 10 nm
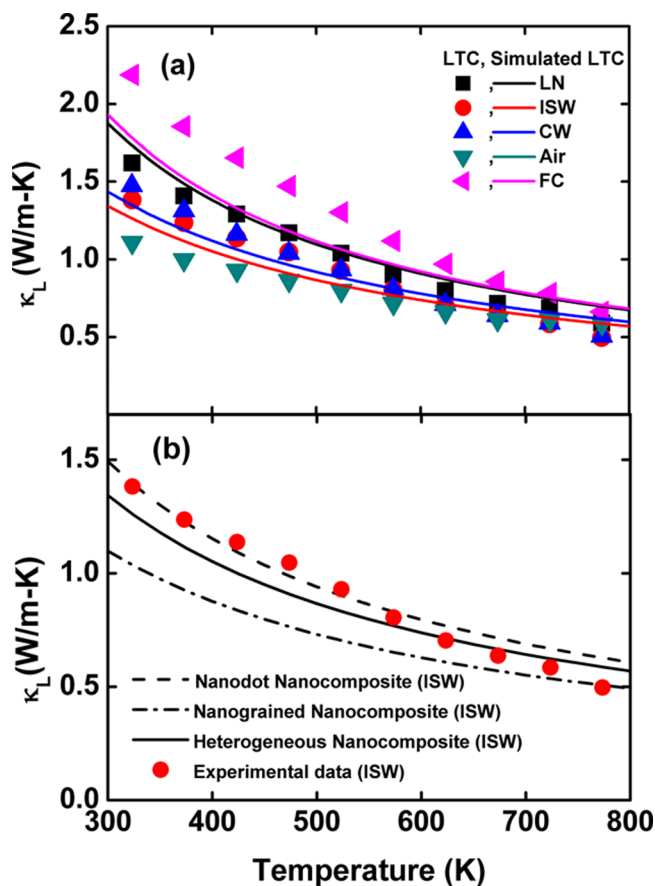
Figure 5. Lattice thermal conductivities, LTC, of (a) QHed pellets showing experimental data and theoretical analysis and (b) the ISW pellet with a prediction for a heterogeneously alloyed nanocomposite. The lattice thermal conductivities of heterogeneous ISW nanocomposite lay between those of nanodot nanocomposites and nanograined nanocomposites.

deduced based on TEM images in Figure 3. The actual data lies somewhere between those two models. In calculating the lattice thermal conductivities of the heterogeneous nanocomposite, we assumed that the nanograined region is 20% based on SEM images and the rest is occupied by the nanodot nanocomposite. The total concentration of nanodots is also fixed at 1.5%, consistent with other samples. However, the actual concentration inside the nanodot nanocomposite is around 1.9% since the nanodots are confined in the nanodot nanocomposite only. Yet, the interparticle distance of 1.5% concentration is around 5.4 nm, and that of 1.9% is 4.9 nm; this reduces the thermal conductivity.

CONCLUSION

In conclusion, we observed heterogeneous nanocomposites (i.e., a mixture of nanodot nanocomposite and nanograined nanocomposite) only in materials quenched with either iced salt water (ISW) or cold water (CW). We found the tiny blobs in the SEM images to be nanograined regions, based on the TEM study of the hot pressed pellets of the materials obtained under different quenching conditions. Surprisingly, these blobs remain unchanged even after annealing the QHed pellets at 773 K for a week. The nanograined regions could have survived during the hot pressing to relieve strain generated due to the lattice mismatch between the PbTe matrix and precipitated nanodots. Further study is required to verify this hypothesis.

The dimensionless thermoelectric figure of merit, zT, for both ISW and CW is around 2.0 at 773 K, which is a 25% increase compared with the zT of FC, i.e. 1.6 at 773 K, which is supposed to be the most homogeneous nanodot nanocomposite in our study. The main reason for such a high zT is due to the thermal conductivity reduction. In the theoretical analysis, we suggested that interparticle distance should decrease due to the fact that under a fixed nanodot concentration, nanodots have to reside in a more confined region compared to the homogeneous nanodot nanocomposites, which reduces phonon mean free path, thereby reducing the thermal conductivity. Also, It is known that thermal conductivity of the heterogeneous material is less than that of the volume averaged thermal conductivity due to the heterogeneous temperature gradient. The heterogeneous nanocomposite could be generated to other materials by the following; Quenching inhibits grain growth leading to produce regions of nanograins. Some of these nanograined regions could be stable in the following synthesis process to relieve strain caused by the lattice mismatch between the matrix and precipitations.

■ ASSOCIATED CONTENT

Ⓢ Supporting Information

Figures show the XRD, calculated quenching time, TEM, HADDF, electrical properties, percentage variations of PF, thermal conductivity and zTs, and theoretical analysis of distribution of nanosize. Table S1 shows the lattice constants and densities for all samples. This material is available free of charge via the Internet at http://pubs.acs.org.

■ AUTHOR INFORMATION

Corresponding Author
*E-mail: woochul@yonsei.ac.kr.

Author Contributions
⊥These authors contributed equally to this work.

Notes
The authors declare no competing financial interest.

■ ACKNOWLEDGMENTS

■ REFERENCES

(1) Rowe, D. M. *CRC Handbook of Thermoelectrics*; CRC Press: 1995.
(2) Rowe, D. M. *CRC Handbook of Thermoelectrics: Macro to Nano*; CRC/Taylor and Francis: 2006.
(3) Shakouri, A. *Annu. Rev. Mater. Res.* **2011**, *41*, 399.
(4) Majumdar, A. *Science* **2004**, *303*, 777.
(5) Vineis, C. J.; Shakouri, A.; Majumdar, A.; Kanatzidis, M. G. *Adv. Mater.* **2010**, *22*, 3970.
(6) Hicks, L. D.; Dresselhaus, M. S. *Phys. Rev. B* **1993**, *47*, 16631.
(7) Hicks, L. D.; Dresselhaus, M. S. *Phys. Rev. B* **1993**, *47*, 12727.
(8) Heremans, J. P.; Jovovic, V.; Toberer, E. S.; Saramat, A.; Kurosaki, K.; Charoenphakdee, A.; Yamanaka, S.; Snyder, G. J. *Science* **2008**, *321*, 554.
(9) Mahan, G. D.; Sofo, J. O. *Proc. Natl. Acad. Sci. U.S.A.* **1996**, *93*, 7436.
(10) Pei, Y.; Shi, X.; LaLonde, A.; Wang, H.; Chen, L.; Snyder, G. J. *Nature* **2011**, *473*, 66.
(11) Kim, W.; Majumdar, A. *J. Appl. Phys.* **2006**, *99*, 084306.
(12) Kim, W.; Singer, S. L.; Majumdar, A.; Zide, J. M. O.; Klenov, D.; Gossard, A. C.; Stemmer, S. *Nano Lett.* **2008**, *8*, 2097.
(13) Kim, W.; Zide, J.; Gossard, A.; Klenov, D.; Stemmer, S.; Shakouri, A.; Majumdar, A. *Phys. Rev. Lett.* **2006**, *96*, 045901.
(14) Biswas, K.; He, J.; Blum, I. D.; Wu, C.-I.; Hogan, T. P.; Seidman, D. N.; Dravid, V. P.; Kanatzidis, M. G. *Nature* **2012**, *489*, 414.
(15) Biswas, K.; He, J.; Zhang, Q.; Wang, G.; Uher, C.; Dravid, V. P.; Kanatzidis, M. G. *Nat. Chem.* **2011**, *3*, 160.
(16) Poudel, B.; Hao, Q.; Ma, Y.; Lan, Y.; Minnich, A.; Yu, B.; Yan, X.; Wang, D.; Muto, A.; Vashaee, D.; Chen, X.; Liu, J.; Dresselhaus, M. S.; Chen, G.; Ren, Z. *Science* **2008**, *320*, 634.
(17) Ohta, M.; Biswas, K.; Lo, S.-H.; He, J.; Chung, D. Y.; Dravid, V. P.; Kanatzidis, M. G. *Adv. Energy Mater.* **2012**, *2*, 1117.
(18) Biswas, K.; He, J. Q.; Wang, G. Y.; Lo, S. H.; Uher, C.; Dravid, V. P.; Kanatzidis, M. G. *Energy Environ. Sci.* **2011**, *4*, 4675.
(19) Klemens, P. G. *Int. J. Thermophys.* **1989**, *10*, 1213.
(20) Klemens, P. G. *J. Appl. Phys.* **1991**, *70*, 4322.
(21) Klemens, P. G. *High Temp. - High Pressures* **1991**, *23*, 241.
(22) Kang, C.; Kim, H.; Park, S.-G.; Kim, W. *Appl. Phys. Lett.* **2010**, *96*, 213114.
(23) Wang, H.; Bahk, J.-H.; Kang, C.; Hwang, J.; Kim, K.; Kim, J.; Burke, P.; Bowers, J.; Gossard, A.; Shakouri, A.; Kim, W. *Proc. Natl. Acad. Sci. U.S.A.* **2014**, *111*, 10949.
(24) Pei, Y.; LaLonde, A.; Iwanaga, S.; Snyder, G. J. *Energy Environ. Sci.* **2011**, *4*, 2085.
(25) Wang, H.; Bahk, J.-H.; Kang, C.; Hwang, J.; Kim, K.; Shakouri, A.; Kim, W. *J. Mater. Chem. A* **2013**, *1*, 11269.
(26) Yamini, S. A.; Ikeda, T.; Lalonde, A.; Pei, Y.; Dou, S. X.; Snyder, G. J. *J. Mater. Chem. A* **2013**, *1*, 8725.
(27) Egorov, Y. P.; Khazanov, I. O.; Root, R. V. *Met. Sci. Heat Treat.* **1983**, *25*, 333.
(28) Baram, M.; Kaplan, W. D. *J. Microsc.* **2008**, *232*, 395.
(29) Blachnik, R.; Igel, R. Z. *Naturforsch., B: J. Chem. Sci.* **1974**, *B 29*, 625.
(30) Callaway, J. *Phys. Rev.* **1959**, *113*, 1046.
(31) Lo, S. H.; He, J. Q.; Biswas, K.; Kanatzidis, M. G.; Dravid, V. P. *Adv. Funct. Mater.* **2012**, *22*, 5175.
(32) Parrott, J. E.; Stuckes, A. D. *Thermal Conductivity of Solids*; Pion: London, 1976.
(33) He, J.; Zhao, L.-D.; Zheng, J.-C.; Doak, J. W.; Wu, H.; Wang, H.-Q.; Lee, Y.; Wolverton, C.; Kanatzidis, M. G.; Dravid, V. P. *J. Am. Chem. Soc.* **2013**, *135*, 4624.
(34) He, J.; Androulakis, J.; Kanatzidis, M. G.; Dravid, V. P. *Nano Lett.* **2011**, *12*, 343.
(35) Blum, I. D.; Isheim, D.; Seidman, D. N.; He, J. Q.; Androulakis, J.; Biswas, K.; Dravid, V. P.; Kanatzidis, M. G. *J. Electron. Mater.* **2012**, *41*, 1583.

High Thermoelectric Performance of a Heterogeneous PbTe Nanocomposite

Hongchao Wang[1,*], Junphil Hwang[1,*], Matthew Loren Snedaker[2], Il-ho Kim[3], Chanyoung Kang[1], Jungwon Kim[1], Galen D. Stucky[2,4], John Bowers[4], Woochul Kim[1,†]

[1]School of Mechanical Engineering, Yonsei University, Seoul 120-749, Korea

[2]Department of Chemistry and Biochemistry, University of California, Santa Barbara, Santa Barbara, California 93106, U.S.A.

[3]Department of Materials Science and Engineering, Korea National University of Transportation, 50 Daehangno, Chungju, Chungbuk 380-702, Korea

[4]Materials Department, University of California, Santa Barbara, Santa Barbara, California 93106, U.S.A.

The powder X-ray diffraction patterns for $Pb_{0.98}Na_{0.02}Te$ samples shown in Figure S1 were collected using Cu Kα radiation at room temperature on the Rigaku powder X-ray diffractometer (XRD) at room temperature. Lattice constants, volumes and theoretical densities were calculated by Rietveld refinement using the Fullprof software. All the peaks of our samples can be indexed to the PbTe structure with an Fm-3m space group, no secondary Na related phase was observed within the limits of XRD, although we found the secondary phase in the TEM images.

The lattice constants, volumes and theoretical densities were calculated based on the XRD data and are shown in Table S1. It was found that the values of lattice constants, volumes and theoretical densities for these 5 samples are almost identical. On the other word, the crystal parameters for $Pb_{0.98}Na_{0.02}Te$ alloys were not affected by different quenching rates. Although there is some error in experimental densities determined by the Archimedes' method, the experimental densities were close to theoretical densities. This indicates the samples were highly densified.

Figure S2 shows estimated quenching time for different quenching media (*i.e.* LN, ISW, CW, Air and FC). We used the lumped capacitance analysis[1] to roughly estimate the quenching rate for simplicity. In the analysis, the melted mixture was approximated as a hot and small solid. Heat from the solid was dissipated through convection heat transfer to the quenching media assuming perfect thermal contact between the solid and the quenching

---

[*] These authors contributed equally to this work

[†] Email: woochul@yonsei.ac.kr

media. However, in reality, vapor blanket occurred in the LN inhibited efficient heat dissipation. The quenching time, the time for the reaction mixture to reach room temperature, was calculated to be about 6, 15 and 30s for LN, ICW, CW, respectively.

The bright field (BF) and high angle annular dark field (HAADF) images shown in Figure S3 clearly suggest the compositional difference at the nano-sized precipitation area. It was Na rich precipitation revealed in recent studies[2-4].

Figure S4 presents the temperature dependence of the electrical resistivities, Seebeck coefficients and power factors for the five $Pb_{0.98}Na_{0.02}Te$ alloys prepared with different quenching rates. All electrical resistivities increased with increasing measured temperature. This metal-like temperature dependence of electrical resistivity was consistent with our previous reports[5,6] on this material. Although the values of electrical resistivities for these five samples were almost the same, some small differences. The electrical resistivities were 4.04, 3.58, 3.59, 3.91 and 3.75 mΩ•cm for the LN, ISW, CW, Air, and FC samples, respectively at the limit of measured temperature. All five samples had positive Seebeck coefficients indicating that the majority of charge carriers are holes, consistent with p-type semiconducting behavior. The S vs T trend basically agrees with the ρ vs T trend. As expected, a sample with lower electrical resistivity normally has a lower Seebeck coefficient.

Figure S5 shows percentage variations in power factors (PF), thermal conductivities (κ) and zTs at 773 K for various quenching rates. All values were normalized to those of FC. As shown in the figure, thermal conductivity reduction ranges from 9% to 15%, yet the power factor increase spans -2% to 5%. Therefore, we can determine that zT increase, which is 7% to 25%, mainly comes from the thermal conductivity reduction. Although it is not clear the difference in PF comes from any scientific reasons or experimental variations, in this paper we focused on the thermal conductivity reduction and assigned detailed reasoning on variations in PF for future study

The sizes of nano-precipitations used in the analysis were 5.5 nm, 2.4 nm, 2.4 nm, 8.5 nm and 8.5 nm for the LN, ISW, CW, Air and FC samples respectively. The sizes were determined based on the TEM pictures as shown in Figure S6 below. To determine the histrogram in Figure S6(b), 4, 6, 5, 2 and 2 TEM pictures for the LN, ISW, CW, Air and FC samples respectively were used. Since we have fixed the concentration of nano-precipitates to be 1.5 % based on the literature value,[7] the size of nano-pricipitates has a direct relationship with the inter-particle spacing – the smaller the size, the closer the inter-particle-spacing. Sensitivity analysis shown in Figure S6(c) was used to understand the effects of size distribution (or inter-particle spacing) on the lattice thermal conductivity. As shown in the figure, variation in the sizes of nano-precipitates in the Air and FC samples affected little on the lattice thermal conductivity, indicating that the effective phonon mean free path should be smaller than 19.3 nm, which is an estimated inter-particle spacing for the Air and FC. As expected, variations of the nano-precipitates and nano-sized grains in 10% respectively changed the lattice thermal conductivity of ISW samples by around 5%. In the ISW sample, we assumed that the nanograined region is 20% based on SEM images. Also, in the theoretical analysis, we assumed that concentration of nano-precipitates is small enough not to change the phonon dispersion.

REFERENCES

(1)   Incropera, F. P.; DeWitt, D. P.; Bergman, T. L.; Lavine, A. *Foundations of heat transfer*; John Wiley & Sons, Inc., 2012.

(2)   Biswas, K.; He, J.; Blum, I. D.; Wu, C.-I.; Hogan, T. P.; Seidman, D. N.; Dravid, V. P.; Kanatzidis, M. G. *Nature* **2012**, *489*, 414.

(3)   Blum, I. D.; Isheim, D.; Seidman, D. N.; He, J. Q.; Androulakis, J.; Biswas, K.; Dravid, V. P.; Kanatzidis, M. G. *Journal of Elec Materi* **2012**, *41*, 1583.

(4)   He, J.; Androulakis, J.; Kanatzidis, M. G.; Dravid, V. P. *Nano Letters* **2011**, *12*, 343.

(5)   Wang, H.; Bahk, J.-H.; Kang, C.; Hwang, J.; Kim, K.; Shakouri, A.; Kim, W. *Journal of Materials Chemistry A* **2013**, *1*, 11269.

(6)   Wang, H.; Bahk, J.-H.; Kang, C.; Hwang, J.; Kim, K.; Kim, J.; Burke, P.; Bowers, J.; Gossard, A.; Shakouri, A.; Kim, W. *Proceedings of the National Academy of Sciences of the United States of America* **2014**, *111*, 10949.

(7)   He, J.; Zhao, L.-D.; Zheng, J.-C.; Doak, J. W.; Wu, H.; Wang, H.-Q.; Lee, Y.; Wolverton, C.; Kanatzidis, M. G.; Dravid, V. P. *Journal of the American Chemical Society* **2013**, *135*, 4624.

Table S1. The lattice constants, volumes, theoretical densities and experimental densities for $Pb_{0.98}Na_{0.02}Te$ samples with five different quenching ratio. For example, a sample with Q-LN denotes $Pb_{0.98}Na_{0.02}Te$ synthesized by quenching into liquid N_2.

Samples	a (Å)	V (Å^3)	Theoretical density (g/cm^3)	Experimental density (g/cm^3)
Q-LN	6.4574	269.26	8.168	8.140
Q-ISW	6.4610	269.71	8.155	8.151
Q-CW	6.4590	269.46	8.162	8.160
Q-Air	6.4607	269.68	8.156	8.012
Q-FC	6.4576	269.29	8.167	8.161
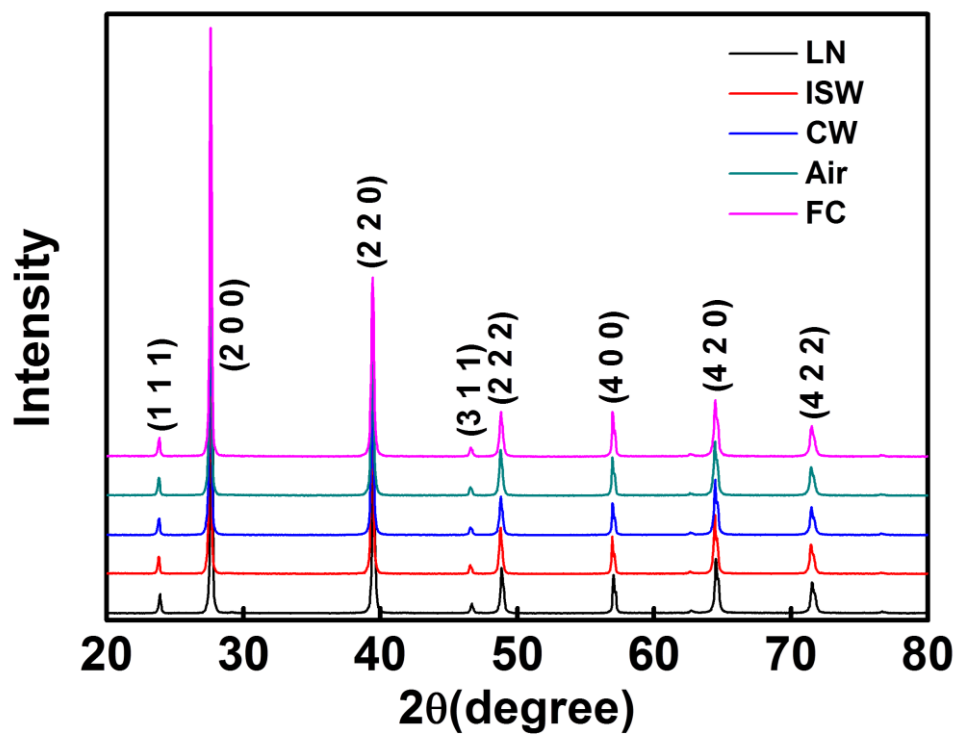
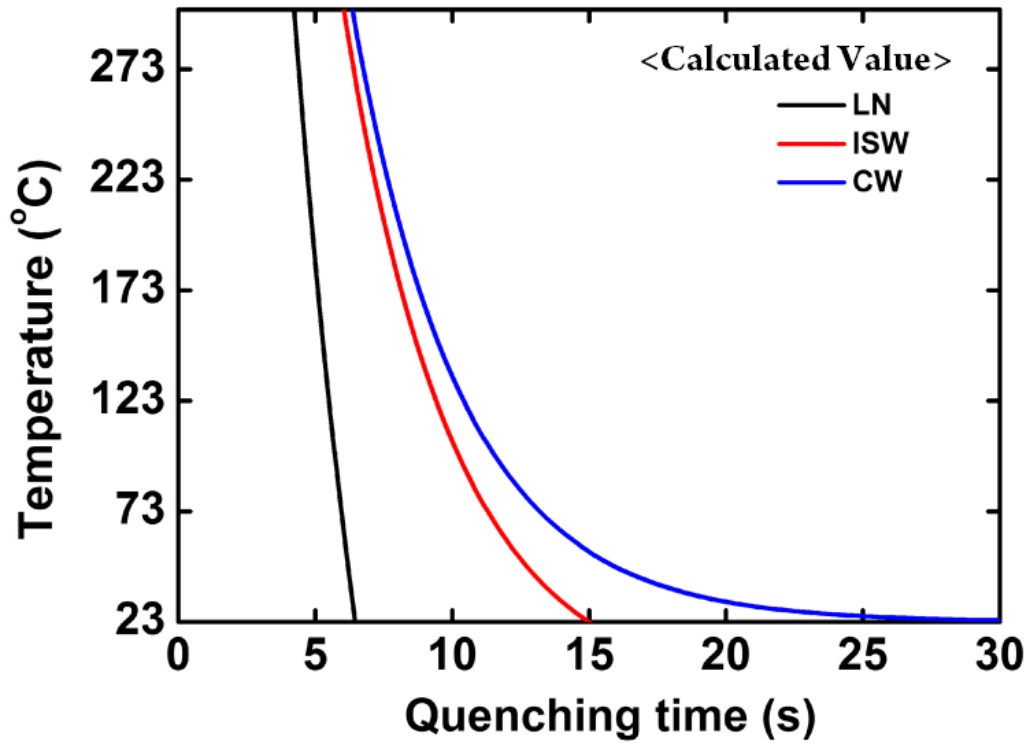Figure S1. The power X-ray diffraction (XRD) patterns for the QHed Pellets.

Figure S2. The temperature versus time graph during quenching process calculated based on the lumped capacitance approximation [1].
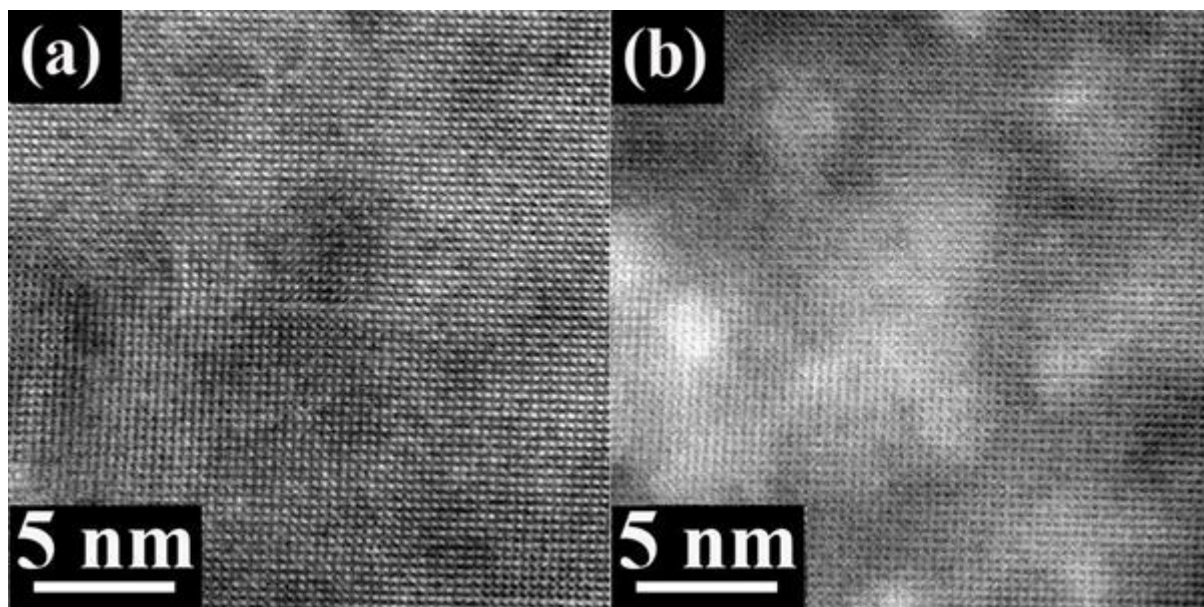
Figure S3. (a) The bright field image of the nanodot nanocomposite region in the CW QHed pellet. (b) The HAADF (high angle annular dark field) image of the the region in (a).
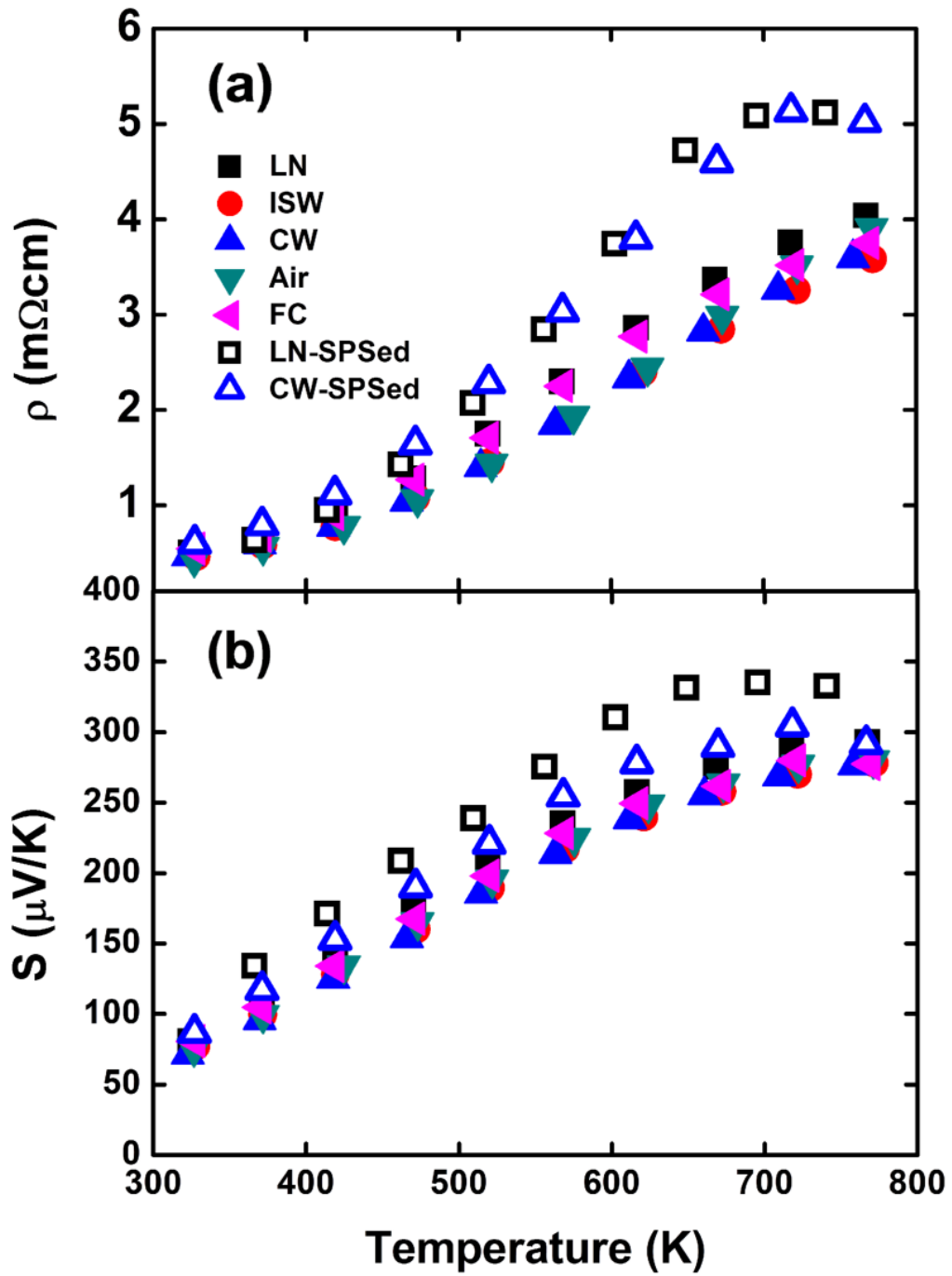
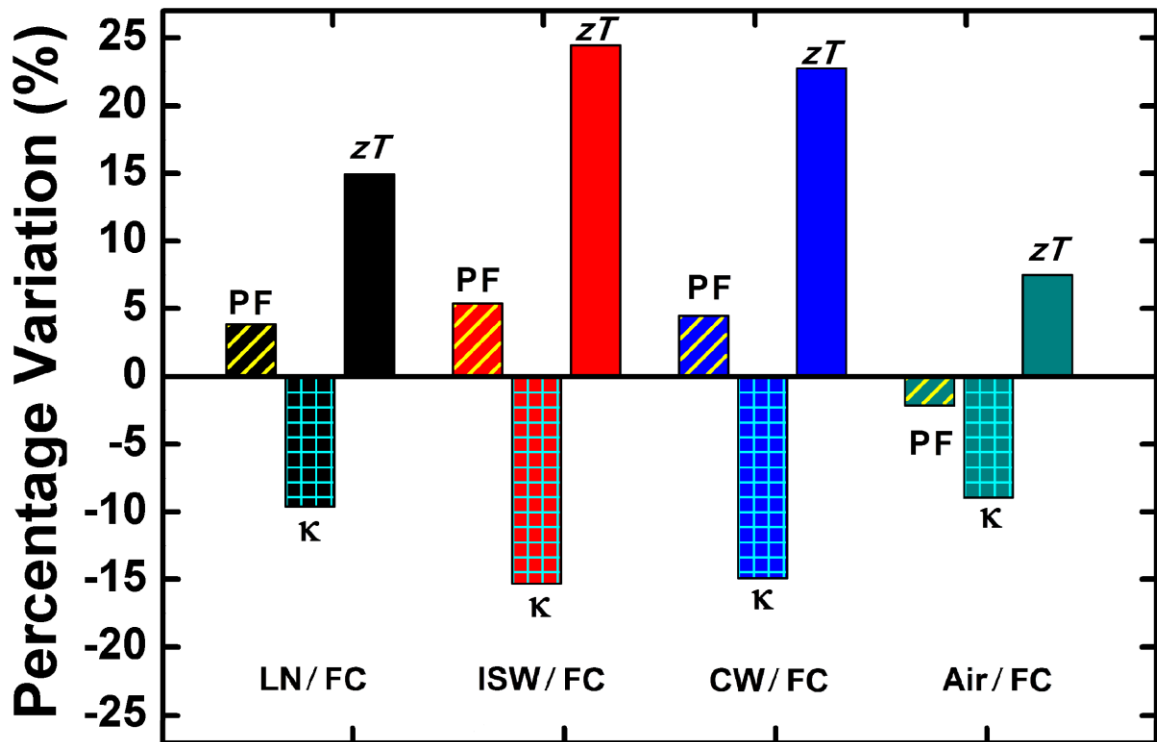Figure S4. (a) Electrical resistivities and (b) Seebeck coefficients of $Pb_{0.98}Na_{0.02}Te$ samples.

Figure S5. Percentage variations of power factors (PF), thermal conductivities (κ), and zTs at 773 K normalized to those of the furnace-cooled samples (FC).
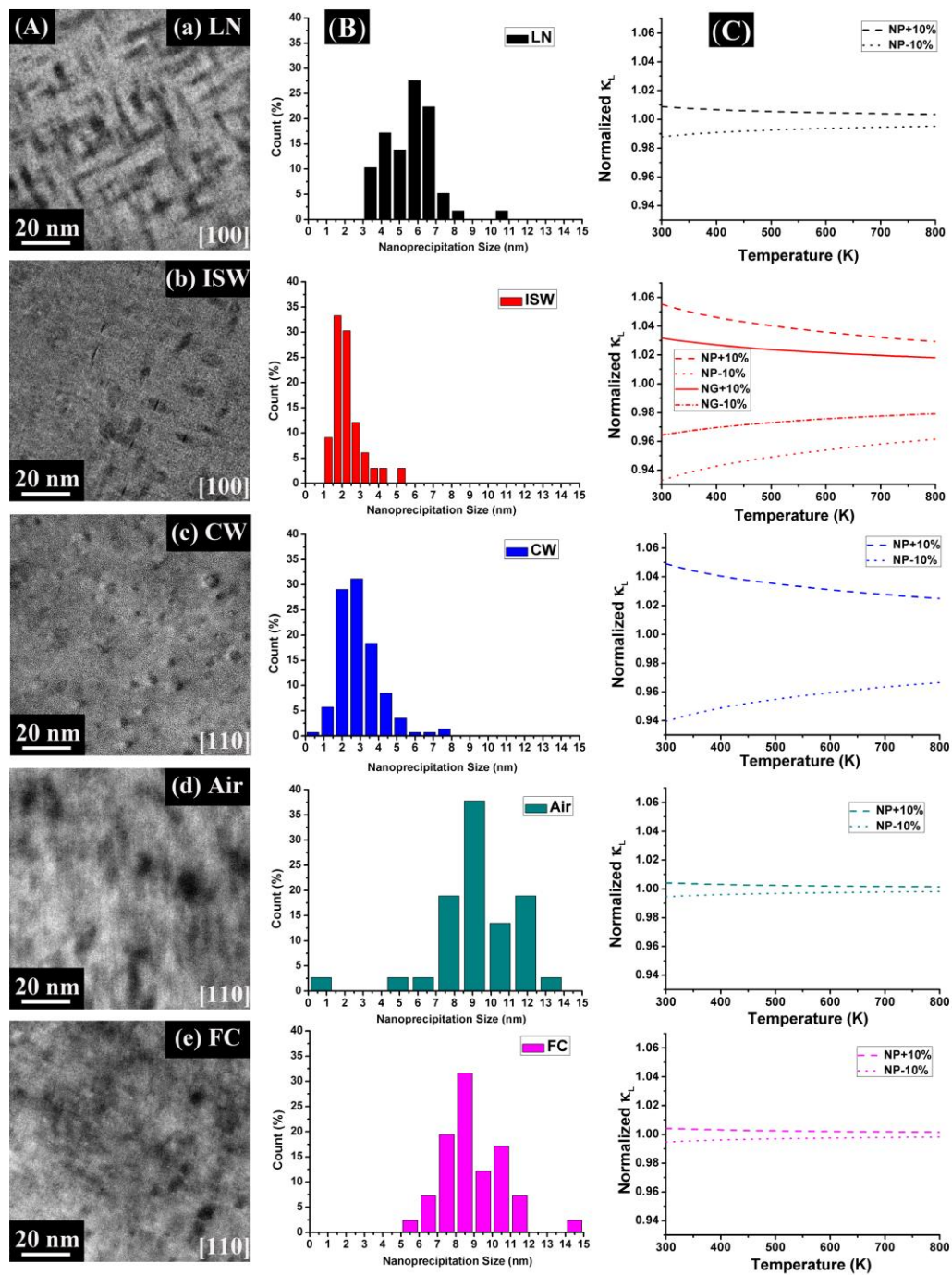
Figure S6. Size distribution of nano-precipitations used in the theoretical analysis; (A) TEM pictures were used for (B) determining size distribution of nanoparticles. In the analysis, 4, 6, 5, 2 and 2 TEM pictures for the LN, ISW, CW, Air and FC samples respectively were used for determining the histogram. Sensitivity analysis on the variation of nanoparticles-sizes (NP) and nano-sized grains (NG) are presented in (C).